Hu, L., Guan, X., Huang, H., Ye, T., Ding, J., Aarti, A., ... & Huang, S. (2024). Assessing the optoelectronic performance of halide perovskite quantum dots with identical bandgaps: composition tuning versus quantum confinement. ACS Energy Letters, 9(8), 3970-3981. This document is the Accepted Manuscript version of a Published Work that appeared in final form in ACS Energy Letters, copyright © 2024 American Chemical Society after peer review and technical editing by the publisher. To access the final edited and published work see https://doi.org/10.1021/acsenergylett.4c01180.

# Assessing the Optoelectronic Performance of Halide Perovskite Quantum Dots with Identical Bandgaps: Composition Tuning vs. Quantum Confinement

Long Hu<sup>1,2#</sup>, Xinwei Guan<sup>3#</sup>, Hehe Huang<sup>4#</sup>, Tingting Ye<sup>5</sup>, Junfeng Ding<sup>5</sup>, Aarti<sup>6</sup>, Koushik Venkatesan<sup>6</sup>, Weizhen Wang<sup>7</sup>, Fandi Chen<sup>1</sup>, Chun-Ho Lin<sup>1</sup>, Tao Wan<sup>1</sup>, Mengyao Li, Jiabao Yi<sup>3</sup>, Rongkun Zheng<sup>8</sup>, Dewei Chu<sup>1\*</sup>, Songhua Cai<sup>7\*</sup>, Jiayi Chen<sup>9</sup>, Claudio Cazorla<sup>10</sup>, Jianyu Yuan<sup>4\*</sup>, Yang Bai<sup>11</sup>, Tom Wu<sup>1,7\*</sup>, Shujuan Huang<sup>2\*</sup>

- <sup>1</sup> School of Materials Science and Engineering, University of New South Wales (UNSW), Sydney, NSW, 2052, Australia
- <sup>2</sup> School of Engineering, Macquarie University Sustainable Energy Research Centre, Macquarie University, Sydney, NSW, 2109, Australia
- <sup>3</sup> Global Innovative Centre for Advanced Nanomaterials, School of Engineering, College of Engineering, Science and Environment, The University of Newcastle, Callaghan, NSW, 2308 Australia
- <sup>4</sup> Institute of Functional Nano & Soft Materials (FUNSOM), Soochow University, Suzhou, Jiangsu 215123, P. R. China
- <sup>5</sup> Key Laboratory of Materials Physics, Institute of Solid-State Physics, Hefei Institutes of Physical Science, Chinese Academy of Sciences, Hefei 230031, China
- <sup>6</sup> School of Natural Sciences, MQ Photonics Research Centre, Macquarie University, Sydney, NSW, 2109, Australia
- <sup>7</sup> Department of Applied Physics, The Hong Kong Polytechnic University, Kowloon, Hong Kong 999077, China
- <sup>8</sup> School of Physics, The University of Sydney, Sydney, NSW 2006, Australia
- <sup>9</sup> School of Molecular and Life Sciences, Curtin University, Bentley, Perth, WA, 6102 Australia
- <sup>10</sup> Departament de Física, Universitat Politècnica de Catalunya, Campus Nord B4-B5, E-08034 Barcelona, Spain
- <sup>11</sup> Faculty of Materials Science and Energy Engineering/Institute of Technology for Carbon Neutrality, Shenzhen Institute of Advanced Technology, Chinese Academy of Sciences, Shenzhen 518055, Guangdong, China

**Email**: d.chu@unsw.edu.au; songhua.cai@polyu.edu.hk; jyyuan@suda.edu.cn; tom.wu@unsw.edu.au; shujuan.huang@mq.edu.au;

Abstract: Halide perovskite quantum dots (QDs) have been considered one of the most promising materials for constructing low-cost high-performing optoelectronics. Tuning the bandgap of perovskite QDs can be accomplished through either size-dependent quantum confinement or altering chemical compositions. To unravel the differences and similarities between these two approaches, two types of QDs, namely CsPbI3 and CsPbI2.5Br0.5 QDs, were synthesized in this study with different sizes but with the same bandgaps of 1.85 eV. Aberration-corrected scanning transmission electron microscopy (STEM) study reveals extensive structural defects and non-perovskite phase in mixed-halide QDs, which correlate with the nonuniform strain distribution. Pressure-dependent photoluminescence (PL) study suggests lower structural stability and distinct lattice distortion in the mixed-halide QDs compared to the pure-halide ones. Furthermore, time-resolved PL and transient absorption measurements indicate longer carrier lifetimes in pure-halide QDs. Finally, the CsPbI<sub>3</sub> QD solar cell delivered a significantly superior power conversion efficiency of 16.1% compared to the mixed halide counterpart (12.8%). Overall, this work provides valuable insights into tailoring quantum confinement and composition engineering strategies for achieving QDs with optimal optoelectronic performance.

**Keywords:** quantum dots, quantum confinement, composition engineering, bandgap, solar cells.

## 1. Introduction

Halide perovskite (ABX<sub>3</sub>) quantum dots (QDs) have been extensively applied in high-performing optoelectronic devices such as photovoltaic cells,<sup>1-9</sup> light-emitting diodes (LEDs),<sup>10-19</sup> detectors,<sup>20-22</sup> lasers,<sup>23-25</sup> and so on.<sup>26-31</sup> One of the most attractive properties of perovskite QDs is their highly tunable optical characteristics, which are suitable for versatile applications.<sup>32-37</sup> The bandgaps of perovskite QDs can be readily and extensively tuned by controlling the compositions of A, B, and X sites.<sup>38,39</sup> Consequently, identical bandgaps can be achieved by various combinations of chemical components such as mixed cations, mixed halides, or their combinations.<sup>40</sup> At the same time, the bandgaps of perovskite QDs can be broadly adjusted by controlling their sizes through the quantum confinement effect.<sup>9,41-43</sup> For instance, perovskite CsPbI<sub>3</sub> bulk film has an intrinsically fixed bandgap of 1.70 eV, while the bandgaps of CsPbI<sub>3</sub> QDs can be flexibly modified from 2.13 eV to 1.73 eV by varying the size of the QDs.<sup>1,44,45</sup>

Given the tunability of QD's bandgaps through chemical compositions or quantum confinement, the question arises regarding which strategy is more effective in achieving desirable photophysical properties while keeping the same bandgaps in the context of solar energy to electricity conversion. Though the identical optical bandgaps of QDs enabled by nanoscale size tuning and composition engineering were reported,<sup>40</sup> their similarities and differences along with their corresponding device performance have not been systematically compared and analyzed. These factors and the extracted insights are expected to play a vital role in advancing the understanding of the QD materials.

In this study, we synthesized two types of halide perovskite QDs, namely CsPbI<sub>3</sub> and CsPbI<sub>2.5</sub>Br<sub>0.5</sub>, with an identical optical bandgap of 1.85 eV via leveraging the quantum confinement effect and the halide composition tuning. Subsequently, the similarities and differences of their physical properties and solar cell performance were systematically

investigated. Extensive structural imperfections and strain were directly observed in the mixed-halide CsPbI<sub>2.5</sub>Br<sub>0.5</sub> QDs, but they are largely absent in the single-halide CsPbI<sub>3</sub> QDs. These findings are in line with the pressure-dependent and steady-state photoluminescence (PL) measurement results. Furthermore, CsPbI<sub>3</sub> QDs exhibited significantly longer carrier lifetimes and faster carrier transfer rates, as characterized by time-resolved PL (TRPL) and transient absorption spectrum (TAS). Finally, the solar cells of CsPbI<sub>3</sub> QDs achieved a significantly superior power conversion efficiency (PCE) of 16.1% compared to the mixed halide counterpart (12.8%). This insight into the QD engineering strategies was further underscored by measurements on two batches of halide perovskite QDs with the same bandgap of 1.95 eV by varying the halide ratio and the QD size.

## 2. Results and Discussion

The perovskite QDs were synthesized using a hot-injection method, as described in Figure 1a. Through tuning QD's composition and size, large-sized CsPbI<sub>2.5</sub>Br<sub>0.5</sub> and small-sized CsPbI<sub>3</sub> QDs exhibit the same optical bandgaps of 1.85 eV (details are given in Supporting Information). As shown in Figure S1a, both QD solutions showed very similar absorption behaviors with the calculated bandgaps of 1.85 eV, and the photos in Figure S1b indicate very similar colors in solutions. Furthermore, photoluminescence quantum yield (PLQY) was measured to be 56% for CsPbI<sub>2.5</sub>Br<sub>0.5</sub> and 84% for CsPbI<sub>3</sub> QDs in purified solution. X-ray photoelectron spectroscopy (XPS) was employed to verify the elemental percentages of QDs. Figure S2 shows the full XPS and elemental core spectra. The elemental percentages are summarized in Table S1, which indicates the stoichiometry of the synthesized QDs consistent with the precursors.

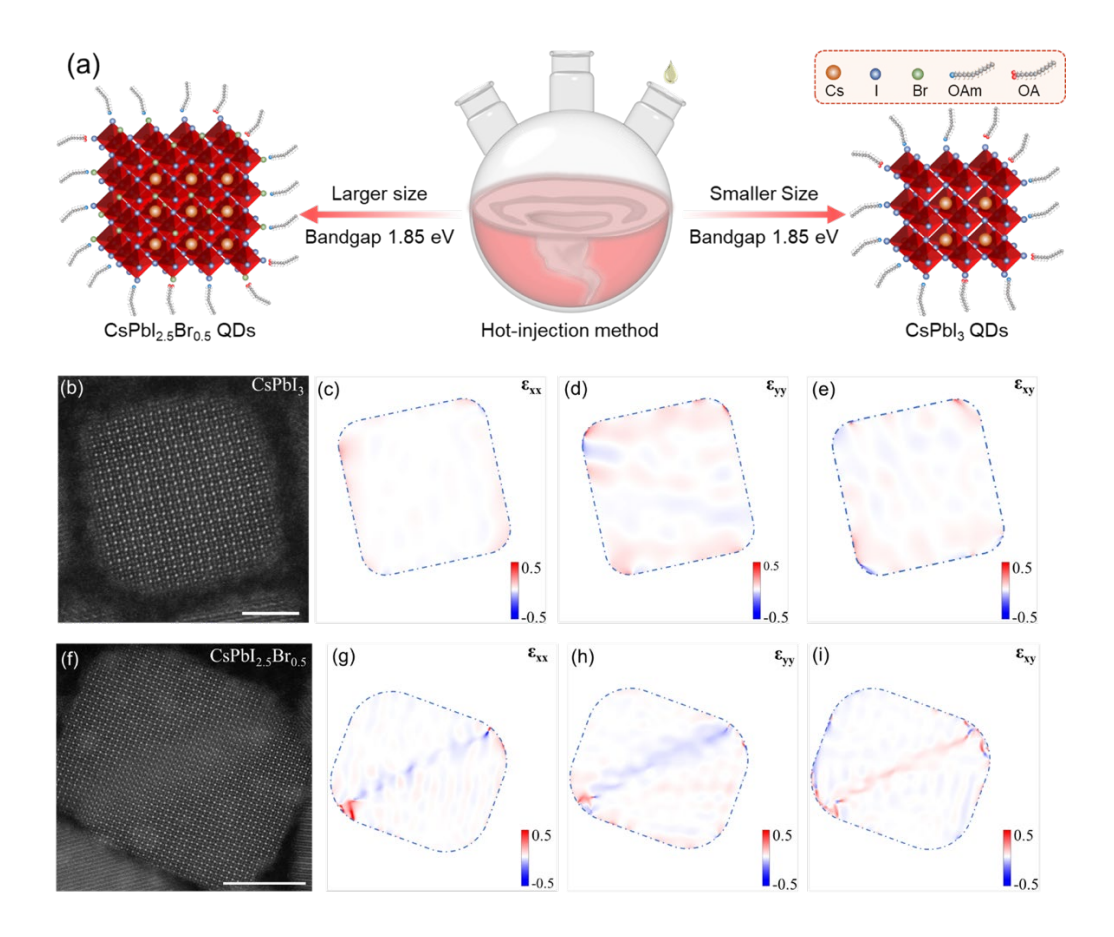


**Figure 1.** (a) Schematic illustration of the process for synthesizing different-sized CsPbI<sub>2.5</sub>Br<sub>0.5</sub> and CsPbI<sub>3</sub> QDs with the same bandgap. CsPbI<sub>3</sub> (b) STEM images, the in-plane strain (c)  $\varepsilon_{xx}$  (d)  $\varepsilon_{yy}$  and (e)  $\varepsilon_{xy}$  distribution in the CsPbI<sub>3</sub> QD, CsPbI<sub>2.5</sub>Br<sub>0.5</sub> QDs (f) STEM image, the in-plane strain (g)  $\varepsilon_{xx}$ , (h)  $\varepsilon_{yy}$  and (i)  $\varepsilon_{yy}$  distribution in the CsPbI<sub>2.5</sub>Br<sub>0.5</sub> QD, as generated by GPA analysis. (Scale bar: 5 nm)

Transmission electron microscopy (TEM) was used to investigate the QD morphologies and size distributions. **Figures S3a** and **b** show that CsPbI<sub>2.5</sub>Br<sub>0.5</sub> and CsPbI<sub>3</sub> QDs possess cubic morphology with a uniform size distribution. The calculated average size is  $12.6 \pm 0.3$  nm for CsPbI<sub>2.5</sub>Br<sub>0.5</sub> and  $9.7 \pm 0.4$  nm for CsPbI<sub>3</sub> QDs, as shown in **Figure S3c** and **3d**, in good agreement with the reported results. <sup>46,47</sup> Notably, both types of QDs demonstrated narrow size distributions, ensuring that the size factor alone would not influence their photophysical properties and device performance. To investigate the atomic structures, aberration-corrected scanning TEM (AC-STEM) was performed, as shown in **Figure S3e-f**. <sup>48</sup> It was observed that extensive atomic-scale defects exist in the mixed halide QDs, as marked by the red circles in

**Figure S3e** while that CsPbI<sub>3</sub> QDs demonstrate a cubic atomic structure without defects (**Figure S3f**). As shown in **Figure S3g**, it was found that the typical defect areas can be classified as lattice defects of perovskite (see **Figure Sg-1**) and non-perovskite phase (see **Figure Sg-1**) existing in the [100] orientated perovskite. Additionally, to investigate the lattice distortions, we performed geometric phase analysis (GPA) based on the atomic-resolution STEM images which can provide the insights for the comparation of both types of QD.<sup>49, 50</sup> As shown in **Figure 1c-e**, all the in-plane strain  $\varepsilon_{xx}$ , the out-of-plane strain  $\varepsilon_{yy}$ , and the xy plane distribution exhibit almost no concentration for CsPbI<sub>3</sub> QDs due to color contrast is very small. However, the existence of defects in CsPbI<sub>2.5</sub>Br<sub>0.5</sub> QDs (**Figure 1f**) leads to remarkable strain concentration across the QD due to color contrast is clear (**Figure 1g-i**). The observed imperfect atomic structures and lattice distortions can presumably cause differences in terms of structural instability under external stimuli, carrier transport and recombination, as well as device performance, which will be discussed in details.

PL behaviors under hydrostatic pressure provide valuable clues to the structures and properties of perovskites without any chemical intervention. <sup>51-54</sup> According to previous works, the bandgap of halide perovskites is primarily determined by the lead and halide orbitals, which are highly sensitive to the change of lattice contraction and tilting of octahedra. <sup>52</sup> Generally, the lattice contraction and octahedra tilting would increase and reduce overlapped orbitals of the constituent elements, resulting in reduced and enlarged bandgaps, respectively. <sup>55</sup> When high pressure is applied to the QDs, both bond length and bond angle might be altered, which in turn affects the PL properties (see **Figure 2a**). This makes hydrostatic pressure a useful tool for investigating the evolution of QD structures. <sup>56</sup>

Prior to the application of pressure, the PL peaks of both types of QDs are located at approximately 670 nm, indicating intrinsic bandgaps of 1.85 eV. However, as the pressure increased, the two types of QDs showed distinct variations in their PL responses (**Figure 2b** 

and **2c**). It is found that the PL peak position of CsPbI<sub>3</sub> QDs initially undergoes a redshift from 669 nm to 676 nm under the pressure from 0 to 0.74 GPa, followed by a blueshift from 676 nm to 644 nm under the pressure from 0.74 GPa to 2.5 GPa. These shifts in the two pressure regimes can be attributed to bond length contraction and bond angle distortion, respectively.<sup>53</sup>, Notably, PL signals could not be detected once the pressure exceeds 2.5 GPa, suggesting a phase transformation of the QDs into an amorphous state without light-emitting properties.<sup>58</sup>

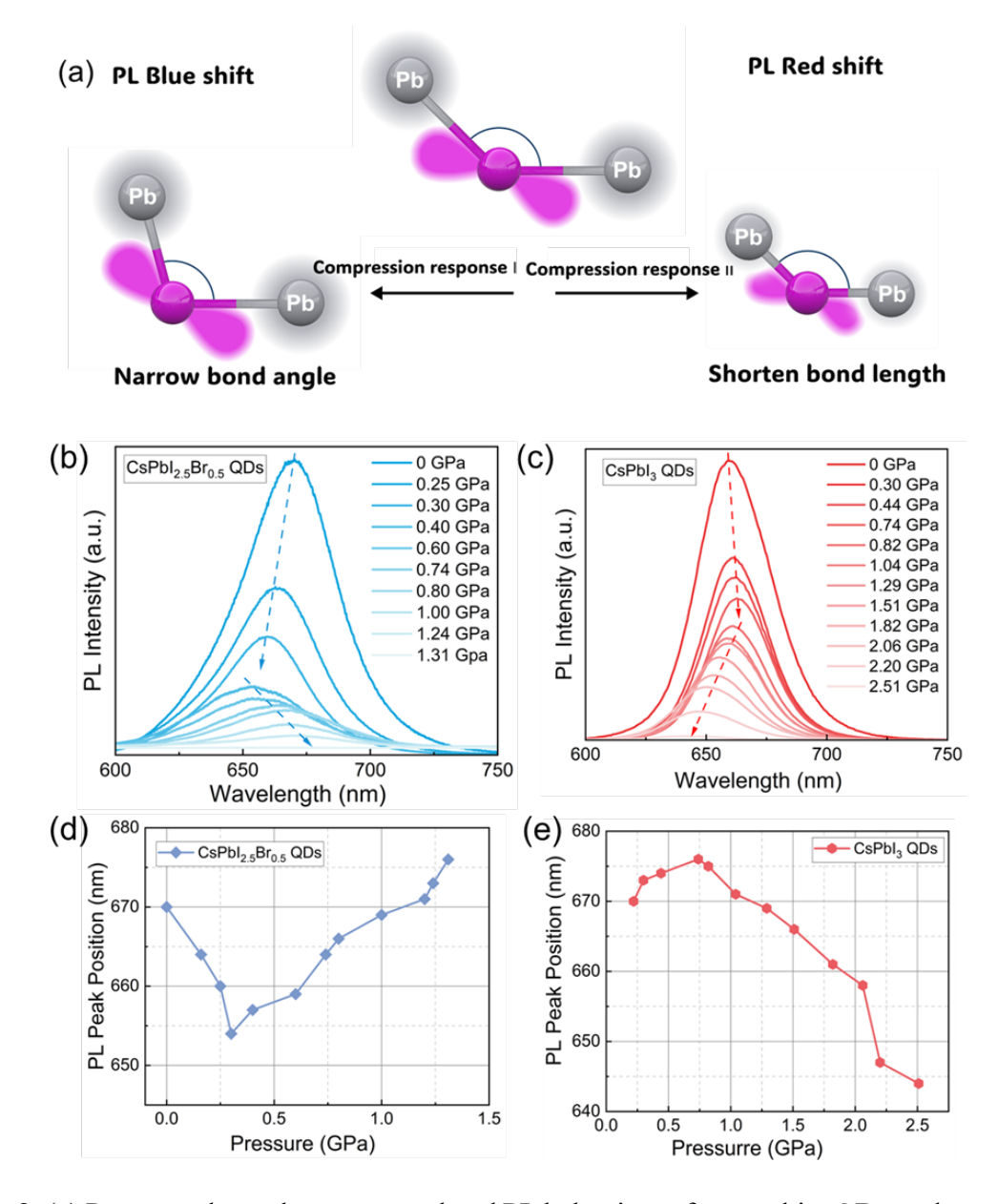


**Figure 2.** (a) Pressure-dependent structural and PL behaviors of perovskite QDs under pressure. PL emission curves of (b) CsPbI<sub>2.5</sub>Br<sub>0.5</sub> QDs and (c) CsPbI<sub>3</sub> QDs under varying pressures. The derived PL peak wavelengths as functions of different pressures for (d) CsPbI<sub>2.5</sub>Br<sub>0.5</sub> QDs and

# (e) CsPbI<sub>3</sub> QDs.

In contrast, for the mixed-halide CsPbI<sub>2.5</sub>Br<sub>0.5</sub> QDs, the PL peak exhibits an initial blueshift from 670 nm to 646 nm under pressure from 0 to 0.39 GPa. Subsequently, the peak gradually redshifts from 646 nm to 676 nm from 0.39 GPa to 1.3 GPa, indicating an evolution of the bond angle distortion and bond length contraction opposite to the CsPbI<sub>3</sub> QDs. Similarly, the PL signals could not be detected upon pressure over 1.3 GPa in the mixed-halide QDs.

The transition pressures to the amorphous state are 2.5 GPa and 1.3 GPa for CsPbI<sub>3</sub> QDs and CsPbI<sub>2.5</sub>Br<sub>0.5</sub> QDs, respectively, indicating that the mixed-halide QDs are more prone to losing long-range ordered structures and transitioning to the amorphous state under pressure. The PL peak evolutions of two types of QDs under pressure are given in **Figure 2d** and **e**. Our results disclose that CsPbI<sub>2.5</sub>Br<sub>0.5</sub> and CsPbI<sub>3</sub> QDs demonstrated different behaviors under pressure. Notably, the pressure-induced PL peaks are reversible, suggesting that both QDs did not degrade during pressure measurements though the PL intensities decreased in both QDs upon the pressure release (see **Figure S4**), which aligns with previous reports.<sup>59-61</sup>

The size of QDs is known to play a critical role in determining the phase transition pressure. Typically, smaller-size halide perovskite QDs exhibit lower transition pressures due to their shorter fluctuation length scales and stronger surface fluctuations. <sup>57,59</sup> However, in our case, we observed that the transition pressure of CsPbI<sub>3</sub> QDs (2.5 GPa) is unexpectedly larger than that of CsPbI<sub>2.5</sub>Br<sub>0.5</sub> QDs (1.3 Gpa), despite the smaller size of CsPbI<sub>3</sub> (9.7 nm) QDs compared to CsPbI<sub>2.5</sub>Br<sub>0.5</sub> QDs (12.6 nm). Previous studies have also reported a transition pressure from the crystalline to amorphous state of CsPbBr<sub>3</sub> QDs at 2.09 Gpa. <sup>54</sup> This suggests that the mixed-halide QDs have lower structural stability against pressure compared to both single-halide CsPbBr<sub>3</sub> and CsPbI<sub>3</sub> QDs, which probably results from the atomic structural imperfections such as non-perovskite phase and defects as evidenced by the spherical aberration corrected TEM images.

Temperature-dependent steady-state PL properties of both types of QDs were further investigated. As shown in **Figure 3a-b**, the normalized PL peaks of both QDs demonstrated a continuous redshift with decreasing temperature from 275K to 77 K, which resulted from an interplay of contributions of the lattice thermal shrinking and electron-phonon coupling. The dominant influence of lattice thermal shrinking resulted in the interaction between orbitals in the valence band maximum, leading to an enlargement in the valence bandwidth and a reduced bandgap.  $^{62-64}$  Since quantum dot sizes vary only slightly between CsPbI<sub>3</sub> QDs (9.7  $\pm$  0.4 nm) and CsPbI<sub>2.5</sub>Br<sub>0.5</sub> QDs (12.6  $\pm$  0.3 nm), the modulation of the Huang-Rhys factor should be negligible. Therefore, the variations of carrier-phonon coupling and Huang-Rhys factor are not invoked in this work.

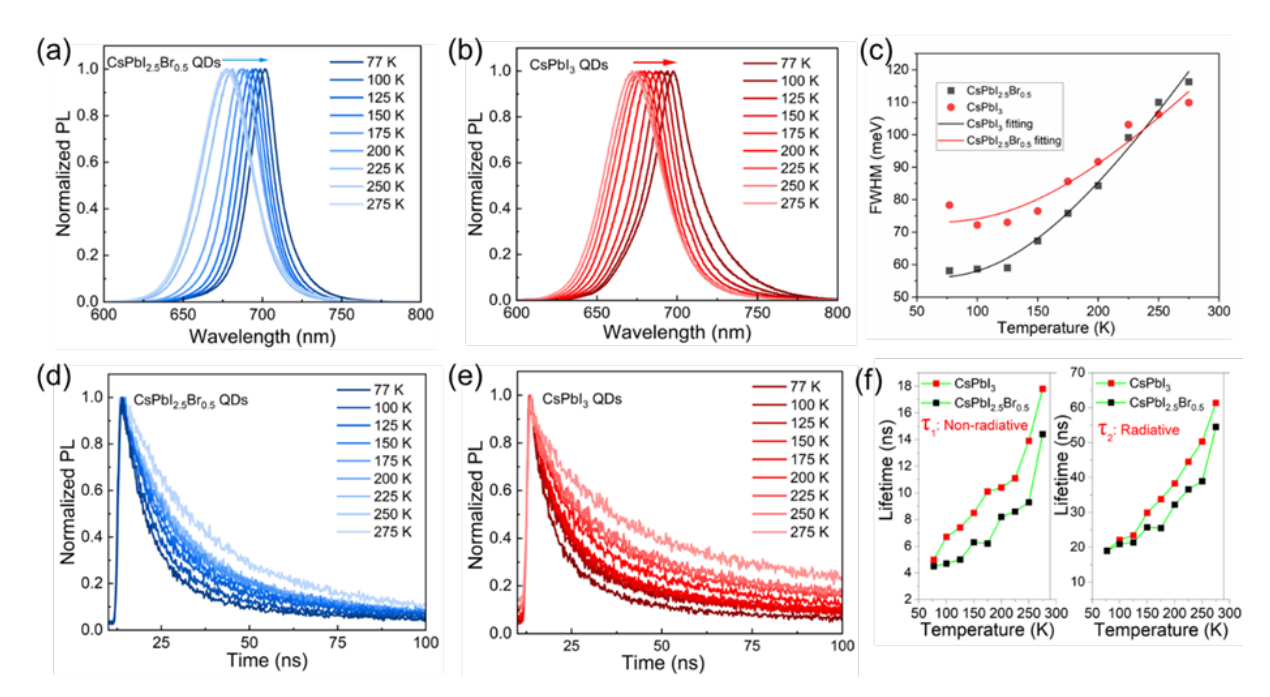


**Figure 3.** Normalized steady-state PL behaviors of (a) CsPbI<sub>2.5</sub>Br<sub>0.5</sub> QDs and (b) CsPbI<sub>3</sub> QDs under different temperatures. (c) PL peak position as a function of temperature for both types of QDs. Normalized TRPL decay curves of (d) CsPbI<sub>2.5</sub>Br<sub>0.5</sub> QDs and (e) CsPbI<sub>3</sub> QDs. (f) Lifetimes τ<sub>1</sub> and τ<sub>2</sub> of these two types of QDs as functions of temperature.

The temperature-dependent full width at half maximum (FWHM) PL intensity data displayed in **Figure 3c** was used to assess the effective strength of coupling to phonons and the contribution from inhomogeneous broadening using the equation:  $\Gamma(T) = \Gamma_{\text{inh}} + \gamma_{ac}T$ 

γιο( $exp(E_{LO}/k_bT) - I$ )- $^I$ . Here,  $\Gamma(T)$  is expressed as the sum of three terms: temperature-independent inhomogeneous broadening ( $\Gamma_{inh}$ ), acoustic ( $\gamma_{ac}T$ ) phonon contributions and temperature-dependent longitudinal optical (LO) phonon scattering ( $\gamma_{LO}(exp(E_{LO}/k_bT) - I)^{-I}$ ).<sup>66</sup>,  $\gamma_{ac}$  represents the coupling strength to acoustic phonons, which is mainly related to a deformation potential interaction in materials with cubic symmetry.  $E_{LO}$  is the energy of the LO phonon, and  $k_B$  is Boltzmann's constant. Through the fitting, the parameters are displayed in **Table 1**, revealing that the contribution of acoustic phonon scattering to PL broadening is zero and photon energy is very similar for both QDs ( $45.1 \pm 15.9$  meV vs.  $42.5 \pm 6.6$  meV). Additionally,  $\Gamma_{inh}$  of CsPbI<sub>3</sub> QDs is larger than that of mixed-halide QDs ( $72.9 \pm 3.2$  meV vs.  $55.7 \pm 2.2$  meV), which is probably due to the fact that the CsPbI<sub>3</sub> QDs have slightly a larger size distribution. Importantly, the longitudinal optical phonon scattering in mixed-halide QDs is much higher than that in CsPbI<sub>3</sub> ( $321.5 \pm 105.3$  meV vs.  $231.9 \pm 179.7$  meV). A higher rate of longitudinal optical phonon scattering would increase the carrier–phonon coupling, leading to increased carrier scattering and non-radiative recombination.

**Table 1**. The extracted parameters by fitting to the temperature-dependent FWHM PL data.

QD Types	$\Gamma_{\text{inh}}$ /meV	$\gamma_{ac}/meV$	$\gamma_{LO}/meV$	ELO /meV
CsPbI <sub>3</sub>	$72.9 \pm 3.2$	0	$231.9 \pm 179.7$	$45.1 \pm 15.9$
CsPbI <sub>2.5</sub> Br <sub>0.5</sub>	$55.7 \pm 2.2$	0	$321.5 \pm 105.3$	$42.5 \pm 6.6$

Moreover, TRPL measurements were performed under varying temperatures. **Figure 3d-e** show the TRPL decay curves of mixed-halide and CsPbI<sub>3</sub> QDs, respectively. A bi-exponential model was used to fit the decay curves to determine  $\tau_1$  and  $\tau_2$ , which represent non-radiative recombination and radiative lifetimes, respectively. As shown in **Figure 3f**, both lifetimes,  $\tau_1$  and  $\tau_2$  monotonously increased with temperature. More importantly, both lifetimes in CsPbI<sub>3</sub> QDs are remarkably longer than those in the mixed-halide counterpart, which is in line with the lower lattice imperfections observed in CsPbI<sub>3</sub> QDs.

Since device applications are often based on film quality, both types of QDs films were prepared on FTO substrates using the same depositing method and were characterized for comparisons. To obtain electronically coupled QD films, insulating organic ligands, including oleic acid and oleylamine of pristine QDs, were removed using methyl acetate (MeOAc) treatment. Initially, Fourier-transform infrared spectroscopy (FTIR) measurements were performed on both QD pristine films (pristine) and ligand removed (LR) films (2 spots measured on the films). As depicted in Figure S5, the signal intensities of C-H modes at 2851 and 2921 cm<sup>-1</sup> are very similar for both QD pristine films and LR films, while they were remarkably reduced in both treated films. This reduction indicates the successful removal of native long-chain ligands following the MeOAc treatment, eliminating the impact of insulating ligands on charge transport.<sup>68</sup> Subsequently, atomic force microscopy (AFM) images (see Figure S6a-b) demonstrate that both QD films have uniform surface morphologies, with an average roughness of 4.12 nm and 4.01 nm for the mixed-halide and CsPbI<sub>3</sub> QD films, respectively. Furthermore, scanning electron microscopy (SEM) characterizations revealed that both QD films were dense and compact without any cracks and pinholes (see Figure S6c-d). These observations of very similar film morphologies eliminate the influence of surface variations as a factor for the different physical properties. Moreover, steady-state PL measurements under continuous laser illumination were carried out on both QD films to investigate their phase segregation behaviors, and the data indicate that phase segregation did not occur in both QD solid films with PL peaks showing no shift (**Figure S7**).

To compare the physical properties of the QD films, UV-vis spectra, and space-charge-limited currency (SCLC) measurements were carried out. **Figure S8a** shows that both QD films have very similar light absorption behaviors, including absorption intensity and range. The defect density calculated from the SCLC data based on the structure of FTO/TiO<sub>2</sub>/QDs/PCBM/Ag is  $6.5 \times 10^{-16}$  cm<sup>-3</sup> and  $3.8 \times 10^{-16}$  cm<sup>-3</sup> for the CsPbI<sub>2.5</sub>Br<sub>0.5</sub> QD film

and CsPbI<sub>3</sub> QD film (**Figure S8b**), respectively, indicating a higher defect density in the mixedhalide QD film, consistent with the TEM and PL measurement results.

To further investigate the carrier dynamic behaviors, TRPL lifetime mappings were conducted on both LR-treated QD films at room temperature (approximately 300 K). The results, as depicted in Figures 4a and b, demonstrate that the carrier lifetime is uniformly distributed in both films. Using bi-exponential fitting of TRPL decay in Figure 4c, the calculated carrier lifetime  $\tau_1$ , representing the carrier recombination rate, is 1.1 ns for CsPbI<sub>2.5</sub>Br<sub>0.5</sub> QD films and 1.4 ns for CsPbI<sub>3</sub> QD films; meanwhile, τ<sub>2</sub>, symbolizing the carrier transfer rate, is measured as 5.1 ns for CsPbI<sub>2.5</sub>Br<sub>0.5</sub> QD films and 3.7 ns for CsPbI<sub>3</sub> QD films.<sup>69,</sup> <sup>70</sup> The carrier lifetime τ<sub>1</sub> in the CsPbI<sub>3</sub> QD film is longer, suggesting that the CsPbI<sub>3</sub> QD film has fewer non-radiative centers, while the carrier lifetime τ<sub>2</sub> in the CsPbI<sub>3</sub> QD film is shorter, facilitating carrier transport and extraction compared to the mixed halide QD film. To gain a deeper understanding of the radiative and non-radiative processes, femtosecond transient absorption (fs-TA) measurements were performed. As shown in Figure 4d, e, the CsPbI<sub>3</sub> QD film exhibits a ground-state bleaching time longer than that of the mixed halide one, demonstrating improved charge separation in this film. The corresponding time-resolved components extracted from the dynamics at 660 nm are shown in Figure 4f. Importantly, CsPbI<sub>3</sub> QD film has a longer decay time relative to the mixed-halide one ( $\tau$ : 2578.7 ps for CsPbI<sub>3</sub> and 1624.3 ps for CsPbI<sub>2.5</sub>Br<sub>0.5</sub>), demonstrating the less non-radiative recombination in the CsPbI<sub>3</sub> QD film. The above results indicate that CsPbI<sub>2.5</sub>Br<sub>0.5</sub> QDs have higher defect density and slower carrier transportation compared to the single-halide counterparts, which is consistent with the differences in their structural and optical properties.

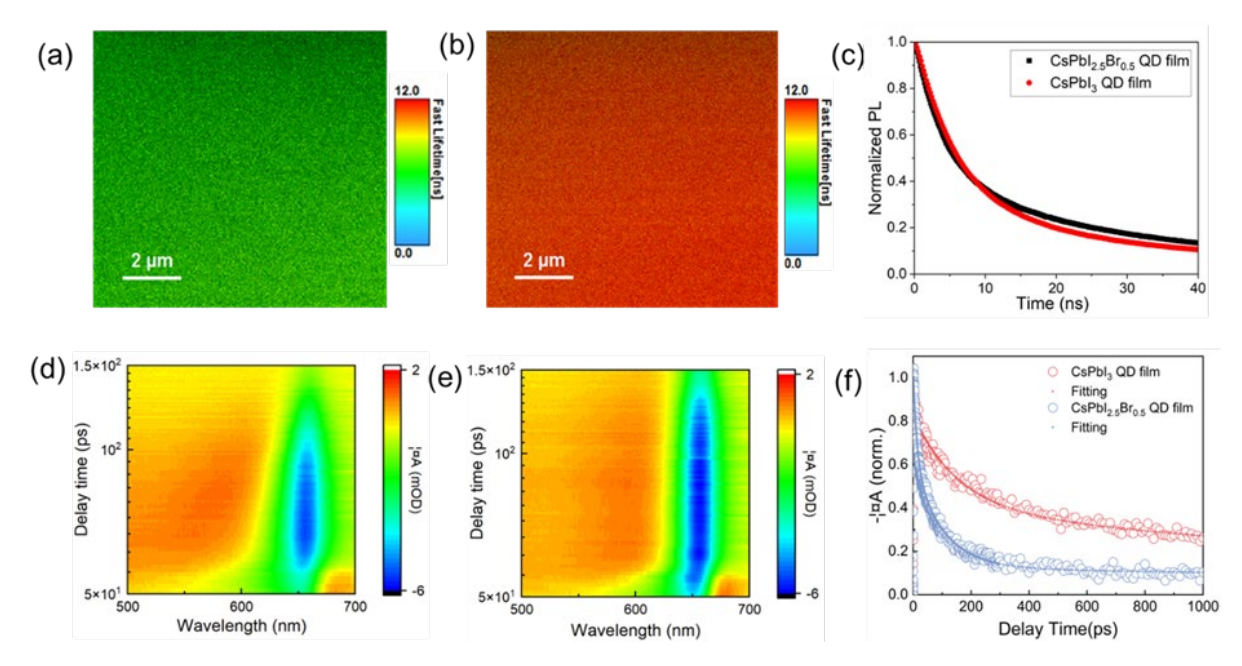


**Figure 4.** Carrier lifetime mapping of (a) CsPbI<sub>2.5</sub>Br<sub>0.5</sub> QD and (b) CsPbI<sub>3</sub> QD films. (c) TRPL decay of both QD films. 2D time-wavelength-dependent TA color maps of (d) CsPbI<sub>2.5</sub>Br<sub>0.5</sub> QD and (e) CsPbI<sub>3</sub> QD films. (f) normalized TA dynamics of the ground-state bleach (GSB: 660 nm) for both QD films.

Considering the critical role of energy levels in device performance, ultra-violet photoelectron spectrum (UPS) was measured to determine the Fermi level and valence band position of both QD films. **Figure S9** shows the UPS spectra of the cutoff and valence band edge regions. The Fermi level,  $\phi = 21.22 - E_{\text{cutoff}}$ , was found to be -4.10 eV and -4.30 eV for the mixed halide QD film and the CsPbI<sub>3</sub> QD film, respectively. In addition, the valence band maximum, VBM =  $21.22 - (E_{\text{cutoff}} - E_{\text{onset}})$ , was calculated to be -5.49 eV for CsPbI<sub>2.5</sub>Br<sub>0.5</sub> QD film and -5.50 eV for the CsPbI<sub>3</sub> QD film. Combining with the bandgaps, the conduction band minimum was located at -3.69 eV for CsPbI<sub>2.5</sub>Br<sub>0.5</sub> QD and -3.70 eV for the CsPbI<sub>3</sub> QD film. From the results above, the Fermi level of CsPbI<sub>3</sub> QD film is located at the middle of the bandgap, which indicates that the CsPbI<sub>3</sub> QD film is more intrinsic than the mixed-halide one, suggesting a lower defect density, in line with the SCLC, TRPL decay and TA results.

First-principles calculations based on density functional theory (DFT) were carried out

to theoretically describe the electronic properties of CsPbI3 and CsPbI2.5Br0.5 QDs as a function of their characteristic size L and the applied pressure (**Figure 5**). The size-dependent trend of theoretical bandgap  $(E_g)$  shown in **Figure 5a** qualitatively mirrors the quantum confinement effects on the optical band gaps that were observed in the experiments. Besides the monotonous decrease, an abrupt shrinking of  $E_g$  is unexpectedly revealed when the QD characteristic size increases from 1.9 to 2.5 nm. We did not calculate for any QD size larger than 2.5 nm due to the constraint of computing power, but the computation result is sufficient to conclude that the confinement effect for large QDs is much weaker compared to the ones with smaller size L. Importantly, the effects of composition on  $E_g$  were also qualitatively reproduced by our DFT calculations. In general, presenting the same optical bandgap, the CsPbI<sub>3</sub> QDs possess a smaller characteristic size than the mixed-halide ones (Figure 5a). More specifically, by applying numerical interpolation to our DFT results, we found that an optical bandgap of 1.8 eV was obtained for CsPbI<sub>3</sub> QDs of L = 3 nm and mixed-halide QDs of L = 12 nm. Although the exact values of L cannot be accurately reproduced by the DFT calculation, the compositiondependent trend of  $E_g$  is consistent with the experimental result. This compositional effect on the optical bandgap is a consequence of the fact that the s-p electronic orbitals of Br ions, whose energy is very close to the top of the valence band, are more localized in space than those of I ions, as shown in the densities of electronic states (Figure 5b-c). Consequently, the optical bandgap of mixed-halide QDs widens up as compared to that of CsPbI<sub>3</sub> QDs, impacting their optoelectronic properties and device performances.

Regarding the influence of pressure on the calculated bandgaps, we observed two different trends in bulk CsPbI<sub>3</sub> and CsPbI<sub>2.5</sub>Br<sub>0.5</sub> (**Figure 5d**). In CsPbI<sub>3</sub>,  $E_g$  first slightly decreases under small compression and then increases almost linearly at pressures larger than ~0.7 GPa. In CsPbI<sub>2.5</sub>Br<sub>0.5</sub>, on the other hand, the band gap monotonously decreases under pressure. These theoretical bandgap results closely resemble our experimental PL

measurements (recall that  $E_g \sim 1/\lambda$ ), except for the redshift observed in the mixed-halide perovskite QDs in the high-pressure regime (Figure 2d). The causes of this compositiondependent discrepancy may be two folds: (1) the distinct polymorphs considered for each material in our DFT calculations (i.e., orthorhombic for CsPbI<sub>3</sub><sup>76, 77</sup> and tetragonal and cubic for CsPbI<sub>2.5</sub>Br<sub>0.5</sub><sup>11, 47, 78</sup>), and (2) an anomalous elastic behavior observed in CsPbI<sub>3</sub> under pressure.<sup>79-81</sup> In particular, we found that the pressure-induced variation of one of the lattice parameters in orthorhombic  $CsPbI_3$  follows the same trend as  $E_g$ , namely it anomalously increases at pressures larger than ~0.7 GPa (Figure 5e). Such an elastic anomaly, namely, da/dP > 0, is not observed in CsPbI<sub>2.5</sub>Br<sub>0.5</sub> (**Figure 5f**). Meanwhile, the variation of the halide octahedra rotation and I-Pb-I and Pb-I-Pb angles in CsPbI3 are continuous and monotonous under compression (Figure 5g-h), in contrast to the elastic anomaly of the lattice parameter. Finally, a conjectural reason for the redshift experimentally observed in CsPbI<sub>2.5</sub>Br<sub>0.5</sub> but not reproduced by our DFT calculations may be related to the presence of halide vacancies (not considered in our  $E_g$  simulations), 82, 83 which according to our DFT formation energy estimations are more likely to form under pressure (Figure 5i). The pressure-induced formation of in-gap defect levels may shrink the bandgap, leading to the experimentally observed redshift in the high-pressure regime.

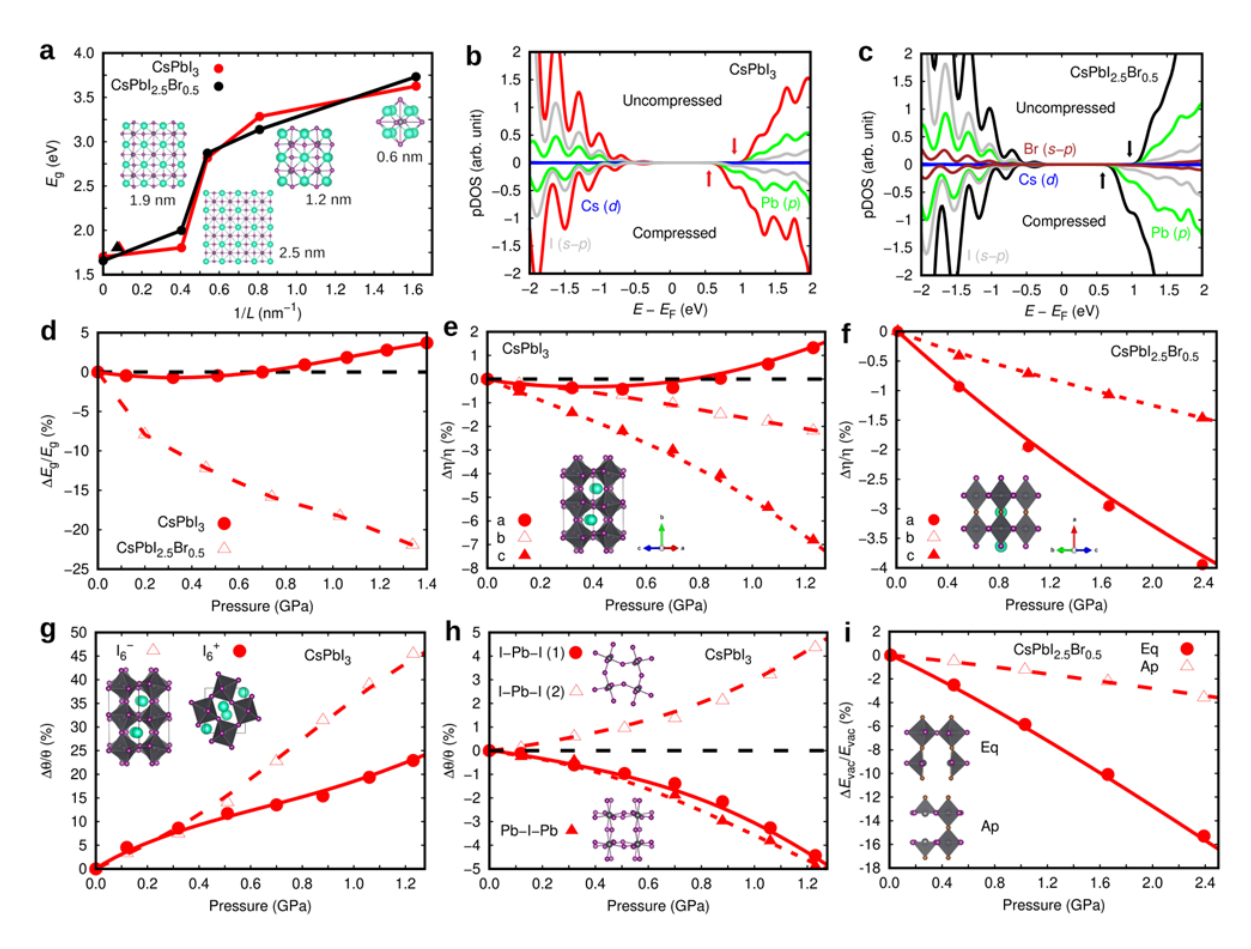
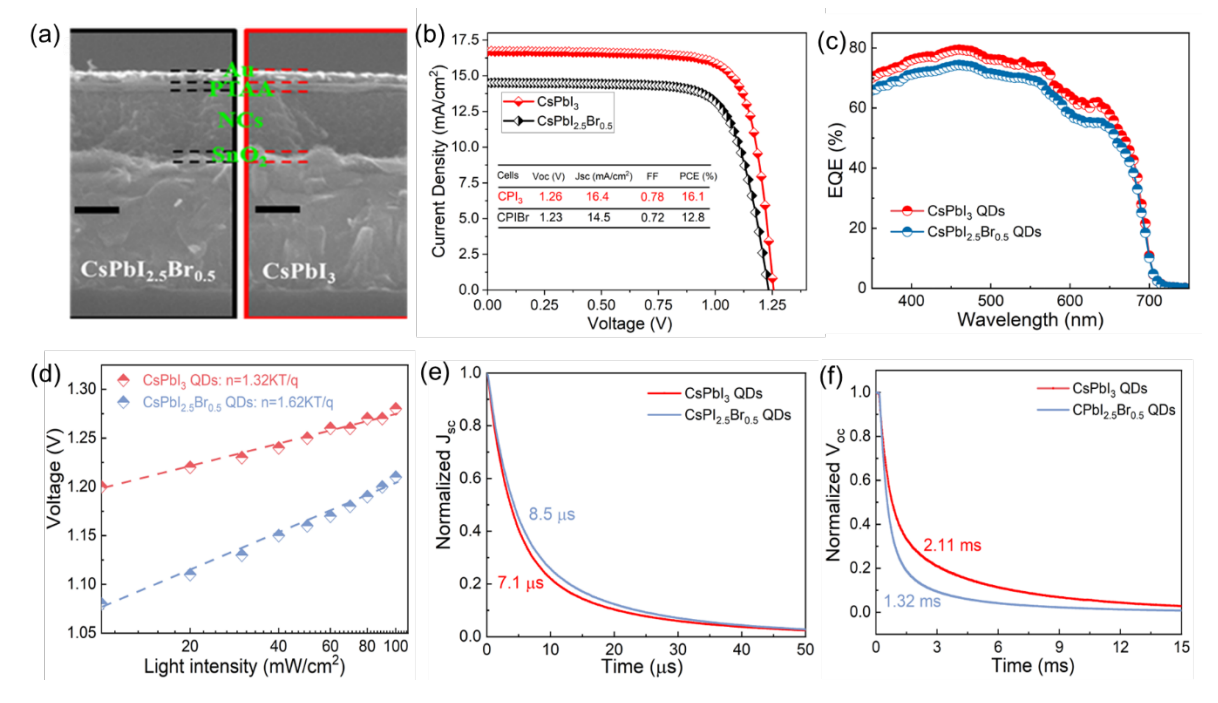


Figure 5. First-principles calculation results based on the density functional theory. (a) Calculated energy band gap of halide perovskite QDs as a function of the inverse of the characteristic length *L*. Experimental  $E_g$  points are indicated with solid triangles. (b) The density of electronic states (DOS) of bulk CsPbI<sub>3</sub> and (c) CsPbI<sub>2.5</sub>Br<sub>0.5</sub> at equilibrium and under pressure. Atomic contributions to the DOS are indicated with different colors and the bottom of the conduction bands with solid arrows. (d) Bandgap of bulk CsPbI<sub>3</sub> and CsPbI<sub>2.5</sub>Br<sub>0.5</sub> as a function of pressure. Lattice parameter variations as induced by pressure in bulk (e) CsPbI<sub>3</sub> and (f) CsPbI<sub>2.5</sub>Br<sub>0.5</sub>. (g) Out-of-phase (I<sub>6</sub><sup>-</sup>) and in-phase (I<sub>6</sub><sup>+</sup>) halide octahedra rotation variations in bulk CsPbI<sub>3</sub> as a function of pressure. (i) Halide vacancy formation energy variation in CsPbI<sub>2.5</sub>Br<sub>0.5</sub> as a function of pressure. "Eq" and "Ap" stand for equatorial and apical point defect positions, respectively. The variations of all quantities are referred to as the corresponding values estimated at zero pressure.

Based on thorough experimental and theoretical characterizations of both QDs, two batches of solar cells were fabricated with an architecture of FTO/TiO<sub>2</sub>/QDs/PTAA/Au to compare their device performance. **Figure 6a** gives the cross-sectional SEM images of the

complete solar cells made from two different QDs. Both batches of solar cells have identical thicknesses of each layer. The energy levels of two types of devices are given in Figure S9c, and the energy levels of TiO<sub>2</sub> and PTAA are from the reported works.<sup>84, 85</sup> Current densityvoltage measurements were carried out to test the device performance, and 21 devices for each batch of solar cells were constructed. As shown in Figure 6b, clearly, all parameters, including voltage (Voc), current density (Jsc), and fill factor (FF), were superior in CsPbI3 solar cells. The champion cells of CsPbI<sub>3</sub> QDs achieved the highest efficiency of 16.1% with a V<sub>oc</sub> of 1.26 V, a J<sub>sc</sub> of 16.4 mA/cm<sup>2</sup>, and an FF of 0.78, while the champion efficiency of CsPbI<sub>2.5</sub>Br<sub>0.5</sub> QD solar cell is 12.8% with a V<sub>oc</sub> of 1.23 V, a J<sub>sc</sub> of 14.5 mA/cm<sup>2</sup>, and an FF of 0.73. The statistics of all device parameters are summarized in **Table 2**, showing that the average efficiency is 15.3% for CsPbI<sub>3</sub> cells and 12.0% for CsPbI<sub>2.5</sub>Br<sub>0.5</sub> devices. To further verify the J<sub>sc</sub>, the external quantum efficiency (EQE) test was performed. As shown in Figure 6c, the CsPbI3 solar cell delivered a higher EQE in the whole response light spectrum, and the integrated J<sub>sc</sub> are 15.5 mA/cm<sup>2</sup> and 13.7 mA/cm<sup>2</sup> for CsPbI<sub>3</sub> and mixed-halide QD devices, respectively. Notably, both devices demonstrated an identical EQE spectrum range, indicating that both QDs have the same electronic bandgap, which is consistent with the light absorption results. However, the Urbach energy calculated from EQE is 25.4 meV for CsPbI<sub>3</sub> and 39.8 meV for the mixed-halide QDs (see Figure S10a), indicating that the defect density is lower in CsPbI<sub>3</sub> QDs than that of mixed-halide QDs. Both types of QD solar cells were measured from forward bias to reverse bias step and from reverse bias to forward step as shown in Figure S10b, showing that there is negligible hysteresis in both types of QD cells.



**Figure 6.** (a) Cross-sectional SEM images of CsPbI<sub>3</sub> and CsPbI<sub>2.5</sub>Br<sub>0.5</sub> QD cells (Scale bar: 200 nm). (b) J-V curves, (c) EQE curves, (d) V<sub>OC</sub> as a function of incident light intensity, (e) TPC, and (f) TPV of both solar cells.

Moreover, in order to gain insight into the charge recombination and charge transport in the QD solar cells, we measured the light intensity-dependent  $V_{oc}$ , transient photovoltage (TPV), and transient photocurrent (TPC) for both solar cells. The light intensity dependence on  $V_{OC}$  follows the relation:  $V_{OC} \propto \eta kT/q$ , where  $\eta kT/q$  is the slope of the light-dependent Voc plot, and depends on the charge recombination mechanism in solar cells. Ref. Ref. Here, K, T, and q are the Boltzmann constant, temperature in Kelvin, and the elemental charge, respectively. Normally, a larger  $\eta$  value indicates the presence of more defect trap states. As shown in Figure 6d, the CsPbI3 cells exhibit a smaller n value compared to that of the mixed-halide cell (1.32 vs 1.62), unravelling that the trap-related recombination was lower in CsPbI3 cells. We use a single exponential function to fit the TPC and TPV decay curves and extract the lifetimes (Figure 6e, f). TPC results show that the CsPbI3 solar cell has a shorter lifetime of 7.1  $\mu$ s, while the CsPbI2.5Br0.5 QD solar cell has a lifetime of 8.5  $\mu$ s, revealing that the CsPbI3 QD solar cell has a higher carrier transport rate. TPV results indicate that the CsPbI3 QD solar cell has a

longer lifetime of 2.11 ms, while the mixed halide solar cell has a lifetime of 1.32 ms, indicating that the CsPbI<sub>3</sub> solar cell has a slower carrier recombination rate. In addition, TPC and TPV results demonstrate that the carrier collection efficiency in the CsPbI<sub>3</sub> solar cell was higher compared with that in the mixed-halide cell. These results hint that the CsPbI<sub>3</sub> QDs are superior in reducing charge recombination loss in cells as a result of the lower defect density, in line with the optical and electrical characterization results.

**Table 2.** Summary of performance statistics for both solar cells. (The champion parameters in parenthesis and 21 devices for each type)

<b>Device Type</b>	V <sub>OC</sub> (V)	J <sub>SC</sub> (mA·cm <sup>-2</sup> )	FF	PCE (%)
CsPbI <sub>3</sub>	$1.25 \pm 0.04 \ (1.26)$	$16.1 \pm 0.6  (16.7)$	$0.76 \pm 0.02 \ (0.78)$	$15.3 \pm 0.5 (16.1)$
CsPbI <sub>2.5</sub> Br <sub>0.5</sub>	$1.20 \pm 0.04 \ (1.23)$	$13.9 \pm 0.7  (14.5)$	$0.72 \pm 0.03 \; (0.73)$	$12.0 \pm 0.5 (12.8)$

To further confirm the universal differences and similarities between the QDs synthesized using quantum confinement effect and composition engineering, two batches of halide perovskite QDs with the same bandgap of 1.95 eV were synthesized, named 1.95-CsPbI3 QDs (size: 6.5 nm) and 1.95-CsPbI2.3Br0.7 QDs (Size:13.9 nm). The comparisons in terms of time-resolved PL, TEM, and solar cell performance are shown in **Figure S11**. First, lattice defects were not observed in 1.95-CsPbI3 QDs but were observed in 1.95-CsPbI2.3Br0.7 QDs. Secondly, carrier lifetime mapping measurements indicated that the average carrier lifetime is longer in 1.95-CsPbI3 QDs than that in 1.95-CsPbI2.3Br0.7 QDs. Moreover, both QD PL peaks are located at 635 nm, suggesting that the bandgaps of both QDs are 1.95 eV. Finally, the champion solar cells of 1.95-CsPbI3 QDs achieved a power conversion efficiency of 12.3% while the counterpart delivered a power conversion efficiency of 9.5%. Therefore, the results obtained in QDs with 1.95 eV bandgaps are consistent with those with 1.85 eV bandgaps, which further gives support to our conclusion on the QD engineering strategies.

#### 3. Conclusion

In summary, we synthesized and extensively investigated two types of all-inorganic

perovskite QDs, i.e., CsPbI<sub>3</sub> and CsPbI<sub>2.5</sub>Br<sub>0.5</sub>. Despite having the same optical bandgaps, these QDs showed different lattice defects, pressure responses, and carrier dynamics. Experimental characterizations and DFT simulations revealed the similarities and differences in perovskite QDs tuned by size and chemical composition engineering. The solar cells made from CsPbI<sub>3</sub> QDs achieved a superior PCE of 16.1%, much higher than that of mixed-halide one (12.8%), which is a result of the coherent lattice structures, suppressed defect density and faster carrier transfer in the single-halide QDs. Armed with these results and valuable insights, further research efforts will propel the advance of judiciously engineered perovskite QDs with tailored properties for next-generation optoelectronic applications.

# **Supporting Information**

Supporting Information is available free of charge.

# **Notes**

The authors declare no competing financial interest.

# Acknowledgements

L.H., X.G., and H.H. contributed equally to this work. L. Hu acknowledges the Australia Research Council (DE230101711). This work was financially supported by the Australian Research Council (DP230101847). C. Lin acknowledges the Australia Research Council (DE240100179). S.C. acknowledges the support of a startup grant from the Department of Applied Physics, the Hong Kong Polytechnic University (1-BDCM), and the Hong Kong Research Grants Council (RGC) General Research Fund (No. 15306122). S. Huang acknowledges the Australia Research Council (LP200200979).

## Reference

- (1) Swarnkar, A.; Marshall, A. R.; Sanehira, E. M.; Chernomordik, B. D.; Moore, D. T.; Christians, J. A.; Chakrabarti, T.; Luther, J. M. Quantum dot-induced phase stabilization of alpha-CsPbI3 perovskite for high-efficiency photovoltaics. *Science* **2016**, *354* (6308), 92-95. DOI: 10.1126/science.aag2700.
- (2) Hao, M.; Bai, Y.; Zeiske, S.; Ren, L.; Liu, J.; Yuan, Y.; Zarrabi, N.; Cheng, N.; Ghasemi, M.; Chen, P. Ligand-assisted cation-exchange engineering for high-efficiency colloidal Cs1-x FA x PbI3 quantum dot solar cells with reduced phase segregation. *Nat. Energy* **2020**, *5* (1), 79-88.
- (3) Hu, L.; Zhao, Q.; Huang, S.; Zheng, J.; Guan, X.; Patterson, R.; Kim, J.; Shi, L.; Lin, C. H.; Lei, Q.; et al. Flexible and efficient perovskite quantum dot solar cells via hybrid interfacial architecture. *Nat. Commun.* **2021**, *12* (1), 466. DOI: 10.1038/s41467-020-20749-1.
- (4) Hu, L.; Li, Q.; Yao, Y.; Zeng, Q.; Zhou, Z.; Cazorla, C.; Wan, T.; Guan, X.; Huang, J.-K.; Lin, C.-H. Perovskite Quantum Dot Solar Cells Fabricated from Recycled Lead-Acid Battery Waste. *ACS Mater. Lett.* **2021**, *4* (1), 120-127.
- (5) Jia, D.; Chen, J.; Qiu, J.; Ma, H.; Yu, M.; Liu, J.; Zhang, X. Tailoring solvent-mediated ligand exchange for CsPbI3 perovskite quantum dot solar cells with efficiency exceeding 16.5%. *Joule* **2022**, *6* (7), 1632-1653.
- (6) Zhang, X.; Huang, H.; Ling, X.; Sun, J.; Jiang, X.; Wang, Y.; Xue, D.; Huang, L.; Chi, L.; Yuan, J.; et al. Homojunction Perovskite Quantum Dot Solar Cells with over 1 microm-Thick Photoactive Layer. *Adv. Mater.* **2022**, *34* (2), e2105977. DOI: 10.1002/adma.202105977.
- (7) Zhao, Q.; Hazarika, A.; Chen, X.; Harvey, S. P.; Larson, B. W.; Teeter, G. R.; Liu, J.; Song, T.; Xiao, C.; Shaw, L.; et al. High efficiency perovskite quantum dot solar cells with charge separating heterostructure. *Nat. Commun.* **2019**, *10* (1), 2842. DOI: 10.1038/s41467-019-10856-z.
- (8) Bai, Y.; Hao, M.; Ding, S.; Chen, P.; Wang, L. Surface Chemistry Engineering of Perovskite Quantum Dots: Strategies, Applications, and Perspectives. *Adv. Mater.* **2022**, *34* (4), e2105958. DOI: 10.1002/adma.202105958.
- (9) Wang, Y.; Zhang, T.; Kan, M.; Li, Y.; Wang, T.; Zhao, Y. Efficient α-CsPbI3 Photovoltaics with Surface Terminated Organic Cations. *Joule* **2018**, *2* (10), 2065-2075. DOI: 10.1016/j.joule.2018.06.013.
- (10) Chiba, T.; Hayashi, Y.; Ebe, H.; Hoshi, K.; Sato, J.; Sato, S.; Pu, Y.-J.; Ohisa, S.; Kido, J. Anion-exchange red perovskite quantum dots with ammonium iodine salts for highly efficient light-emitting devices. *Nat. Photonics* **2018**, *12* (11), 681-687. DOI: 10.1038/s41566-018-0260-y.
- (11) Wang, Y. K.; Singh, K.; Li, J. Y.; Dong, Y.; Wang, X. Q.; Pina, J. M.; Yu, Y. J.; Sabatini, R.; Liu, Y.; Ma, D.; et al. In Situ Inorganic Ligand Replenishment Enables Bandgap Stability in Mixed-Halide Perovskite Quantum Dot Solids. *Adv. Mater.* **2022**, *34* (21), e2200854. DOI: 10.1002/adma.202200854.
- (12) Wu, X. G.; Ji, H.; Yan, X.; Zhong, H. Industry outlook of perovskite quantum dots for display applications. *Nat. Nanotechnol.* **2022**, *17* (8), 813-816. DOI: 10.1038/s41565-022-01163-8.
- (13) Dong, Y.; Wang, Y. K.; Yuan, F.; Johnston, A.; Liu, Y.; Ma, D.; Choi, M. J.; Chen, B.; Chekini, M.; Baek, S. W.; et al. Bipolar-shell resurfacing for blue LEDs based on strongly confined perovskite quantum dots. *Nat. Nanotechnol.* **2020**, *15* (8), 668-674. DOI: 10.1038/s41565-020-0714-5.
- (14) Xu, L.; Li, J.; Cai, B.; Song, J.; Zhang, F.; Fang, T.; Zeng, H. A bilateral interfacial passivation strategy promoting efficiency and stability of perovskite quantum dot light-emitting diodes. *Nat. Commun.* **2020**, *11* (1), 3902. DOI: 10.1038/s41467-020-17633-3.
- (15) Lan, Y. F.; Yao, J. S.; Yang, J. N.; Song, Y. H.; Ru, X. C.; Zhang, Q.; Feng, L. Z.; Chen, T.;

- Song, K. H.; Yao, H. B. Spectrally Stable and Efficient Pure Red CsPbI(3) Quantum Dot Light-Emitting Diodes Enabled by Sequential Ligand Post-Treatment Strategy. *Nano Lett.* **2021**, *21* (20), 8756-8763. DOI: 10.1021/acs.nanolett.1c03011.
- (16) Zheng, X.; Yuan, S.; Liu, J.; Yin, J.; Yuan, F.; Shen, W.-S.; Yao, K.; Wei, M.; Zhou, C.; Song, K.; et al. Chlorine Vacancy Passivation in Mixed Halide Perovskite Quantum Dots by Organic Pseudohalides Enables Efficient Rec. 2020 Blue Light-Emitting Diodes. *ACS Energy Lett.* **2020**, *5* (3), 793-798. DOI: 10.1021/acsenergylett.0c00057.
- (17) Tan, Z. K.; Moghaddam, R. S.; Lai, M. L.; Docampo, P.; Higler, R.; Deschler, F.; Price, M.; Sadhanala, A.; Pazos, L. M.; Credgington, D.; et al. Bright light-emitting diodes based on organometal halide perovskite. *Nat. Nanotechnol.* **2014**, *9* (9), 687-692. DOI: 10.1038/nnano.2014.149.
- (18) Wang, R.; Xiang, H.; Li, Y.; Zhou, Y.; Shan, Q.; Su, Y.; Li, Z.; Wang, Y.; Zeng, H. Minimizing Energy Barrier in Intermediate Connection Layer for Monolithic Tandem WPeLEDs with Wide Color Gamut. *Adv. Funct. Mater.* **2023**, *33* (21), 2215189. DOI: 10.1002/adfm.202215189.
- (19) Song, J.; Li, J.; Li, X.; Xu, L.; Dong, Y.; Zeng, H. Quantum Dot Light-Emitting Diodes Based on Inorganic Perovskite Cesium Lead Halides (CsPbX3). *Adv. Mater.* **2015**, *27* (44), 7162-7167. DOI: 10.1002/adma.201502567.
- (20) Chen, Q.; Wu, J.; Ou, X.; Huang, B.; Almutlaq, J.; Zhumekenov, A. A.; Guan, X.; Han, S.; Liang, L.; Yi, Z.; et al. All-inorganic perovskite nanocrystal scintillators. *Nature* **2018**, *561* (7721), 88-93. DOI: 10.1038/s41586-018-0451-1.
- (21) Xu, Q.; Zhou, S.; Huang, J.; Ouyang, X.; Liu, J.; Guo, Y.; Wang, J.; Nie, J.; Zhang, X.; Ouyang, X.; et al. Ultra-flexible and highly sensitive scintillation screen based on perovskite quantum dots for non-flat objects X-ray imaging. *Mater. Today Phys.* **2021**, *18*, 100390. DOI: 10.1016/j.mtphys.2021.100390.
- (22) Liu, J.; Shabbir, B.; Wang, C.; Wan, T.; Ou, Q.; Yu, P.; Tadich, A.; Jiao, X.; Chu, D.; Qi, D.; et al. Flexible, Printable Soft-X-Ray Detectors Based on All-Inorganic Perovskite Quantum Dots. *Adv. Mater.* **2019**, *31* (30), e1901644. DOI: 10.1002/adma.201901644.
- (23) Tian, J.; Tan, Q. Y.; Wang, Y.; Yang, Y.; Yuan, G.; Adamo, G.; Soci, C. Perovskite quantum dot one-dimensional topological laser. *Nat. Commun.* **2023**, *14* (1), 1433. DOI: 10.1038/s41467-023-36963-6.
- (24) Chen, J.; Du, W.; Shi, J.; Li, M.; Wang, Y.; Zhang, Q.; Liu, X. Perovskite quantum dot lasers. *InfoMat* **2019**, *2* (1), 170-183. DOI: 10.1002/inf2.12051.
- (25) Wang, Y.; Li, X.; Song, J.; Xiao, L.; Zeng, H.; Sun, H. All-Inorganic Colloidal Perovskite Quantum Dots: A New Class of Lasing Materials with Favorable Characteristics. *Adv. Mater.* **2015**, *27* (44), 7101-7108. DOI: 10.1002/adma.201503573.
- (26) Lin, J.; Lu, Y.; Li, X.; Huang, F.; Yang, C.; Liu, M.; Jiang, N.; Chen, D. Perovskite Quantum Dots Glasses Based Backlit Displays. *ACS Energy Lett.* **2021**, *6* (2), 519-528. DOI: 10.1021/acsenergylett.0c02561.
- (27) Singh, S.; Chen, H.; Shahrokhi, S.; Wang, L. P.; Lin, C.-H.; Hu, L.; Guan, X.; Tricoli, A.; Xu, Z. J.; Wu, T. Hybrid Organic–Inorganic Materials and Composites for Photoelectrochemical Water Splitting. *ACS Energy Lett.* **2020**, *5* (5), 1487-1497. DOI: 10.1021/acsenergylett.0c00327.
- (28) Younis, A.; Lin, C. H.; Guan, X.; Shahrokhi, S.; Huang, C. Y.; Wang, Y.; He, T.; Singh, S.; Hu, L.; Retamal, J. R. D.; et al. Halide Perovskites: A New Era of Solution-Processed Electronics. *Adv. Mater.* **2021**, *33* (23), e2005000. DOI: 10.1002/adma.202005000.
- (29) Li, X.; Hu, X.; Li, C.; Yang, W.; Wang, C.; Chen, Y.; Zeng, H. Are Inorganic Lead Halide Perovskite Nanocrystals Promising Scintillators? *ACS Energy Lett.* **2023**, *8* (7), 2996-3004. DOI: 10.1021/acsenergylett.3c00920.
- (30) Kim, J.; Hu, L.; Chen, H.; Guan, X.; Anandan, P. R.; Li, F.; Tang, J.; Lin, C.-H.; Kalantar-

- Zadeh, K.; Tricoli, A.; et al. P-type Charge Transport and Selective Gas Sensing of All-Inorganic Perovskite Nanocrystals. *ACS Mater. Lett.* **2020**, *2* (11), 1368-1374. DOI: 10.1021/acsmaterialslett.0c00346.
- (31) Kim, J.; John, A. T.; Li, H.; Huang, C. Y.; Chi, Y.; Anandan, P. R.; Murugappan, K.; Tang, J.; Lin, C. H.; Hu, L.; et al. High-Performance Optoelectronic Gas Sensing Based on All-Inorganic Mixed-Halide Perovskite Nanocrystals with Halide Engineering. *Small Methods* **2024**, *8* (2), e2300417. DOI: 10.1002/smtd.202300417.
- (32) Huang, C. Y.; Li, H.; Wu, Y.; Lin, C. H.; Guan, X.; Hu, L.; Kim, J.; Zhu, X.; Zeng, H.; Wu, T. Inorganic Halide Perovskite Quantum Dots: A Versatile Nanomaterial Platform for Electronic Applications. *Nano-Micro Lett.* **2022**, *15* (1), 16. DOI: 10.1007/s40820-022-00983-6.
- (33) Duan, L.; Hu, L.; Guan, X.; Lin, C. H.; Chu, D.; Huang, S.; Liu, X.; Yuan, J.; Wu, T. Quantum Dots for Photovoltaics: A Tale of Two Materials. *Adv. Energy Mater.* **2021**, *11* (20), 2100354. DOI: 10.1002/aenm.202100354.
- (34) Ummadisingu, A.; Meloni, S.; Mattoni, A.; Tress, W.; Gratzel, M. Crystal-Size-Induced Band Gap Tuning in Perovskite Films. *Angew. Chem., Int. Ed.* **2021**, *60* (39), 21368-21376. DOI: 10.1002/anie.202106394.
- (35) Zhou, Y.; Fang, T.; Liu, G.; Xiang, H.; Yang, L.; Li, Y.; Wang, R.; Yan, D.; Dong, Y.; Cai, B.; et al. Perovskite Anion Exchange: A Microdynamics Model and a Polar Adsorption Strategy for Precise Control of Luminescence Color. *Adv. Funct. Mater.* **2021**, *31* (51), 2106871. DOI: 10.1002/adfm.202106871.
- (36) Zhou, Y.; Jia, Y. H.; Fang, H. H.; Loi, M. A.; Xie, F. Y.; Gong, L.; Qin, M. C.; Lu, X. H.; Wong, C. P.; Zhao, N. Composition-Tuned Wide Bandgap Perovskites: From Grain Engineering to Stability and Performance Improvement. *Adv. Funct. Mater.* **2018**, *28* (35), 1803130. DOI: 10.1002/adfm.201803130.
- (37) Li, X.; Wu, Y.; Zhang, S.; Cai, B.; Gu, Y.; Song, J.; Zeng, H. CsPbX3 Quantum Dots for Lighting and Displays: Room-Temperature Synthesis, Photoluminescence Superiorities, Underlying Origins and White Light-Emitting Diodes. *Adv. Funct. Mater.* **2016**, *26* (15), 2435-2445. DOI: 10.1002/adfm.201600109.
- (38) Suri, M.; Hazarika, A.; Larson, B. W.; Zhao, Q.; Vallés-Pelarda, M.; Siegler, T. D.; Abney, M. K.; Ferguson, A. J.; Korgel, B. A.; Luther, J. M. Enhanced Open-Circuit Voltage of Wide-Bandgap Perovskite Photovoltaics by Using Alloyed (FA1–x Cs x) Pb (I1–x Br x) 3 Quantum Dots. *ACS Energy Lett.* **2019**, *4* (8), 1954-1960.
- (39) McMeekin, D. P.; Sadoughi, G.; Rehman, W.; Eperon, G. E.; Saliba, M.; Horantner, M. T.; Haghighirad, A.; Sakai, N.; Korte, L.; Rech, B.; et al. A mixed-cation lead mixed-halide perovskite absorber for tandem solar cells. *Science* **2016**, *351* (6269), 151-155. DOI: 10.1126/science.aad5845.
- (40) Gil-Escrig, L.; Dreessen, C.; Palazon, F.; Hawash, Z.; Moons, E.; Albrecht, S.; Sessolo, M.; Bolink, H. J. Efficient Wide-Bandgap Mixed-Cation and Mixed-Halide Perovskite Solar Cells by Vacuum Deposition. *ACS Energy Lett* **2021**, *6* (2), 827-836. DOI: 10.1021/acsenergylett.0c02445.
- (41) Liu, F.; Zhang, Y.; Ding, C.; Kobayashi, S.; Izuishi, T.; Nakazawa, N.; Toyoda, T.; Ohta, T.; Hayase, S.; Minemoto, T.; et al. Highly Luminescent Phase-Stable CsPbI(3) Perovskite Quantum Dots Achieving Near 100% Absolute Photoluminescence Quantum Yield. *ACS Nano* **2017**, *11* (10), 10373-10383. DOI: 10.1021/acsnano.7b05442.
- (42) Yuan, J.; Bi, C.; Xi, J.; Guo, R.; Tian, J. Gradient-Band Alignment Homojunction Perovskite Quantum Dot Solar Cells. *J Phys Chem Lett* **2021**, *12* (3), 1018-1024. DOI: 10.1021/acs.jpclett.0c03628.
- (43) Protesescu, L.; Yakunin, S.; Bodnarchuk, M. I.; Krieg, F.; Caputo, R.; Hendon, C. H.; Yang, R. X.; Walsh, A.; Kovalenko, M. V. Nanocrystals of Cesium Lead Halide Perovskites

- (CsPbX(3), X = Cl, Br, and I): Novel Optoelectronic Materials Showing Bright Emission with Wide Color Gamut. *Nano Lett.* **2015**, *15* (6), 3692-3696. DOI: 10.1021/nl5048779.
- (44) Khan, J.; Zhang, X.; Yuan, J.; Wang, Y.; Shi, G.; Patterson, R.; Shi, J.; Ling, X.; Hu, L.; Wu, T.; et al. Tuning the Surface-Passivating Ligand Anchoring Position Enables Phase Robustness in CsPbI3 Perovskite Quantum Dot Solar Cells. *ACS Energy Lett.* **2020**, *5* (10), 3322-3329. DOI: 10.1021/acsenergylett.0c01849.
- (45) Li, F.; Zhou, S.; Yuan, J.; Qin, C.; Yang, Y.; Shi, J.; Ling, X.; Li, Y.; Ma, W. Perovskite Quantum Dot Solar Cells with 15.6% Efficiency and Improved Stability Enabled by an α-CsPbI3/FAPbI3 Bilayer Structure. *ACS Energy Lett.* **2019**, *4* (11), 2571-2578. DOI: 10.1021/acsenergylett.9b01920.
- (46) Ling, X.; Zhou, S.; Yuan, J.; Shi, J.; Qian, Y.; Larson, B. W.; Zhao, Q.; Qin, C.; Li, F.; Shi, G. 14.1% CsPbI3 perovskite quantum dot solar cells via cesium cation passivation. *Adv. Energy Mater.* **2019**, *9* (28), 1900721.
- (47) Liu, Y.; Li, Q.; Zhang, W.; Yang, Z.; Zhao, S.; Chen, W. CsPbI3 Perovskite Quantum Dot Solar Cells with Both High Efficiency and Phase Stability Enabled by Br Doping. *ACS Appl. Energy Mater.* **2021**, *4* (7), 6688-6696. DOI: 10.1021/acsaem.1c00750.
- (48) Ma, M.; Zhang, X.; Xu, L.; Chen, X.; Wang, L.; Cheng, T.; Wei, F.; Yuan, J.; Shen, B. Atomically Unraveling the Structural Evolution of Surfaces and Interfaces in Metal Halide Perovskite Quantum Dots. *Adv. Mater.* **2023**, *35* (31), e2300653. DOI: 10.1002/adma.202300653.
- (49) Cai, S.; Dai, J.; Shao, Z.; Rothmann, M. U.; Jia, Y.; Gao, C.; Hao, M.; Pang, S.; Wang, P.; Lau, S. P.; et al. Atomically Resolved Electrically Active Intragrain Interfaces in Perovskite Semiconductors. *J. Am. Chem. Soc.* **2022**, *144* (4), 1910-1920. DOI: 10.1021/jacs.1c12235.
- (50) Guo, S.; Zhang, X.; Hao, M.; Duan, T.; Wang, W.; Li, Z.; Liu, G.; Cai, S.; Zhou, Y. Liquid-Phase Transfer of Organic–Inorganic Halide Perovskite Films for TEM Investigation and Planar Heterojunction Fabrication. *Adv. Opt. Mater.* **2023**, *12* (8), 2301255. DOI: 10.1002/adom.202301255.
- (51) Zhang, L.; Liu, C.; Wang, L.; Liu, C.; Wang, K.; Zou, B. Pressure-Induced Emission Enhancement, Band-Gap Narrowing, and Metallization of Halide Perovskite Cs(3) Bi(2) I(9). *Angew. Chem., Int. Ed.* **2018**, *57* (35), 11213-11217. DOI: 10.1002/anie.201804310.
- (52) Beimborn, J. C.; Hall, L. M. G.; Tongying, P.; Dukovic, G.; Weber, J. M. Pressure Response of Photoluminescence in Cesium Lead Iodide Perovskite Nanocrystals. *J. Phys. Chem. C* **2018**, *122* (20), 11024-11030. DOI: 10.1021/acs.jpcc.8b03280.
- (53) Cao, Y.; Qi, G.; Liu, C.; Wang, L.; Ma, Z.; Wang, K.; Du, F.; Xiao, G.; Zou, B. Pressure-Tailored Band Gap Engineering and Structure Evolution of Cubic Cesium Lead Iodide Perovskite Nanocrystals. *J. Phys. Chem. C* **2018**, *122* (17), 9332-9338. DOI: 10.1021/acs.jpcc.8b01673.
- (54) Xiao, G.; Cao, Y.; Qi, G.; Wang, L.; Liu, C.; Ma, Z.; Yang, X.; Sui, Y.; Zheng, W.; Zou, B. Pressure Effects on Structure and Optical Properties in Cesium Lead Bromide Perovskite Nanocrystals. *J. Am. Chem. Soc.* **2017**, *139* (29), 10087-10094. DOI: 10.1021/jacs.7b05260.
- (55) Gao, X.; Wang, Q.; Zhang, Y.; Cui, C.; Sui, N.; Chi, X.; Zhang, H.; Zhou, Q.; Bao, Y.; Wang, Y. Pressure Effects on Optoelectronic Properties of CsPbBr3 Nanocrystals. *J. Phys. Chem. C* **2020**, *124* (20), 11239-11247. DOI: 10.1021/acs.jpcc.0c02701.
- (56) Wang, L.; Wang, K.; Zou, B. Pressure-Induced Structural and Optical Properties of Organometal Halide Perovskite-Based Formamidinium Lead Bromide. *J Phys Chem Lett* **2016**, 7 (13), 2556-2562. DOI: 10.1021/acs.jpclett.6b00999.
- (57) Beimborn, J. C., 2nd; Walther, L. R.; Wilson, K. D.; Weber, J. M. Size-Dependent Pressure-Response of the Photoluminescence of CsPbBr(3) Nanocrystals. *J Phys Chem Lett* **2020**, *11* (5), 1975-1980. DOI: 10.1021/acs.jpclett.0c00174.
- (58) Zhang, L.; Wang, K.; Lin, Y.; Zou, B. Pressure Effects on the Electronic and Optical

- Properties in Low-Dimensional Metal Halide Perovskites. *J Phys Chem Lett* **2020**, *11* (12), 4693-4701. DOI: 10.1021/acs.jpclett.0c01014.
- (59) Vukovic, O.; Folpini, G.; Wong, E. L.; Leoncino, L.; Terraneo, G.; Albaqami, M. D.; Petrozza, A.; Cortecchia, D. Structural effects on the luminescence properties of CsPbI(3) nanocrystals. *Nanoscale* **2023**, *15* (12), 5712-5719. DOI: 10.1039/d2nr06345j.
- (60) Gong, J.; Zhong, H.; Gao, C.; Peng, J.; Liu, X.; Lin, Q.; Fang, G.; Yuan, S.; Zhang, Z.; Xiao, X. Pressure-Induced Indirect-Direct Bandgap Transition of CsPbBr(3) Single Crystal and Its Effect on Photoluminescence Quantum Yield. *Adv. Sci.* **2022**, *9* (29), e2201554. DOI: 10.1002/advs.202201554.
- (61) Tian, M.; Gao, Y.; Zhou, P.; Chi, K.; Zhang, Y.; Liu, B. Improving persistent luminescence in pressure-tuned CsPbBr(3) nanocrystals by Ce(3+) doping. *Phys. Chem. Chem. Phys.* **2021**, 23 (36), 20567-20573. DOI: 10.1039/d1cp02864b.
- (62) Cherrette, V. L.; Babbe, F.; Cooper, J. K.; Zhang, J. Z. Octahedral Distortions Generate a Thermally Activated Phonon-Assisted Radiative Recombination Pathway in Cubic CsPbBr(3) Perovskite Quantum Dots. *J Phys Chem Lett* **2023**, *14* (39), 8717-8725. DOI: 10.1021/acs.jpclett.3c02568.
- (63) Ma, Z.; Liu, Z.; Lu, S.; Wang, L.; Feng, X.; Yang, D.; Wang, K.; Xiao, G.; Zhang, L.; Redfern, S. A. T.; et al. Pressure-induced emission of cesium lead halide perovskite nanocrystals. *Nat. Commun.* **2018**, *9* (1), 4506. DOI: 10.1038/s41467-018-06840-8.
- (64) Zhang, L.; Zeng, Q.; Wang, K. Pressure-Induced Structural and Optical Properties of Inorganic Halide Perovskite CsPbBr(3). *J Phys Chem Lett* **2017**, *8* (16), 3752-3758. DOI: 10.1021/acs.jpclett.7b01577.
- (65) Liu, X. Y.; Cui, Y.; Deng, J. P.; Liu, Y. Y.; Ma, X. F.; Hou, Y. X.; Wei, J. Y.; Li, Z. Q.; Wang, Z. W. Charge Carriers Trapping by the Full-Configuration Defects in Metal Halide Perovskites Quantum Dots. *J Phys Chem Lett* **2022**, *13* (38), 8858-8863. DOI: 10.1021/acs.jpclett.2c02311. (66) Shinde, A.; Gahlaut, R.; Mahamuni, S. Low-Temperature Photoluminescence Studies of CsPbBr3 Quantum Dots. *J. Phys. Chem. C* **2017**, *121* (27), 14872-14878. DOI: 10.1021/acs.jpcc.7b02982.
- (67) Cheng, O. H.; Qiao, T.; Sheldon, M.; Son, D. H. Size- and temperature-dependent photoluminescence spectra of strongly confined CsPbBr(3) quantum dots. *Nanoscale* **2020**, *12* (24), 13113-13118, 10.1039/D0NR02711A. DOI: 10.1039/d0nr02711a.
- (68) Han, R.; Zhao, Q.; Su, J.; Zhou, X.; Ye, X.; Liang, X.; Li, J.; Cai, H.; Ni, J.; Zhang, J. Role of Methyl Acetate in Highly Reproducible Efficient CsPbI3 Perovskite Quantum Dot Solar Cells. *J. Phys. Chem. C* **2021**, *125* (16), 8469-8478. DOI: 10.1021/acs.jpcc.0c09057.
- (69) Ren, A.; Lai, H.; Hao, X.; Tang, Z.; Xu, H.; Yu Jeco, B. M. F.; Watanabe, K.; Wu, L.; Zhang, J.; Sugiyama, M.; et al. Efficient Perovskite Solar Modules with Minimized Nonradiative Recombination and Local Carrier Transport Losses. *Joule* **2020**, *4* (6), 1263-1277. DOI: 10.1016/j.joule.2020.04.013.
- (70) Khan, J. I.; Isikgor, F. H.; Ugur, E.; Raja, W.; Harrison, G. T.; Yengel, E.; Anthopoulos, T. D.; De Wolf, S.; Laquai, F. Charge Carrier Recombination at Perovskite/Hole Transport Layer Interfaces Monitored by Time-Resolved Spectroscopy. *ACS Energy Lett.* **2021**, *6* (12), 4155-4164. DOI: 10.1021/acsenergylett.1c01931.
- (71) Hu, L.; Zhang, Z.; Patterson, R. J.; Hu, Y.; Chen, W.; Chen, C.; Li, D.; Hu, C.; Ge, C.; Chen, Z.; et al. Achieving high-performance PbS quantum dot solar cells by improving hole extraction through Ag doping. *Nano Energy* **2018**, *46*, 212-219. DOI: 10.1016/j.nanoen.2018.01.047.
- (72) Hu, L.; Guan, X.; Wan, T.; Lin, C.-H.; Liu, S.; Zhu, R.; Chen, W.; Yao, Y.; Huang, C.-Y.; Yuan, L.; et al. Valence-Regulated Metal Doping of Mixed-Halide Perovskites to Modulate Phase Segregation and Solar Cell Performance. *ACS Energy Lett.* **2022**, *7* (12), 4150-4160. DOI: 10.1021/acsenergylett.2c02040.

- (73) Hu, L.; Duan, L.; Yao, Y.; Chen, W.; Zhou, Z.; Cazorla, C.; Lin, C. H.; Guan, X.; Geng, X.; Wang, F.; et al. Quantum Dot Passivation of Halide Perovskite Films with Reduced Defects, Suppressed Phase Segregation, and Enhanced Stability. *Adv. Sci.* **2022**, *9* (2), e2102258. DOI: 10.1002/advs.202102258.
- (74) Hu, L.; Guan, X.; Chen, W.; Yao, Y.; Wan, T.; Lin, C.-H.; Pham, N. D.; Yuan, L.; Geng, X.; Wang, F.; et al. Linking Phase Segregation and Photovoltaic Performance of Mixed-Halide Perovskite Films through Grain Size Engineering. *ACS Energy Lett.* **2021**, *6* (4), 1649-1658. DOI: 10.1021/acsenergylett.1c00213.
- (75) Cazorla, C.; Boronat, J. Simulation and understanding of atomic and molecular quantum crystals. *Rev. Mod. Phys.* **2017**, *89* (3), 035003. DOI: 10.1103/RevModPhys.89.035003.
- (76) Jia, D.; Chen, J.; Zhuang, R.; Hua, Y.; Zhang, X. Antisolvent-Assisted In Situ Cation Exchange of Perovskite Quantum Dots for Efficient Solar Cells. *Adv. Mater.* **2023**, *35* (21), e2212160. DOI: 10.1002/adma.202212160.
- (77) Li, Y.; Wang, L.; Xiang, D.; Zhu, J.; Wu, K. Dielectric and Wavefunction Engineering of Electron Spin Lifetime in Colloidal Nanoplatelet Heterostructures. *Adv. Sci.* **2024**, *11* (12), e2306518. DOI: 10.1002/advs.202306518.
- (78) Ke, F.; Wang, C.; Jia, C.; Wolf, N. R.; Yan, J.; Niu, S.; Devereaux, T. P.; Karunadasa, H. I.; Mao, W. L.; Lin, Y. Preserving a robust CsPbI(3) perovskite phase via pressure-directed octahedral tilt. *Nat. Commun.* **2021**, *12* (1), 461. DOI: 10.1038/s41467-020-20745-5.
- (79) Li, Z.-G.; Zacharias, M.; Zhang, Y.; Wei, F.; Qin, Y.; Yang, Y.-Q.; An, L.-C.; Gao, F.-F.; Li, W.; Even, J.; et al. Origin of Phase Transitions in Inorganic Lead Halide Perovskites: Interplay between Harmonic and Anharmonic Vibrations. *ACS Energy Lett.* **2023**, *8* (7), 3016-3024. DOI: 10.1021/acsenergylett.3c00881.
- (80) Gao, L. K.; Tang, Y. L. Theoretical Study on the Carrier Mobility and Optical Properties of CsPbI(3) by DFT. *ACS Omega* **2021**, *6* (17), 11545-11555. DOI: 10.1021/acsomega.1c00734.
- (81) Aktary, M.; Kamruzzaman, M.; Afrose, R. Pressure-dependent comparative study of the mechanical, electronic, and optical properties of CsPbX 3 (X= Cl, Br, I): a DFT study for optoelectronic applications. *Mater. Adv.* **2023**, *4* (19), 4494-4508.
- (82) Pan, J.; Li, X.; Gong, X.; Yin, J.; Zhou, D.; Sinatra, L.; Huang, R.; Liu, J.; Chen, J.; Dursun, I.; et al. Halogen Vacancies Enable Ligand-Assisted Self-Assembly of Perovskite Quantum Dots into Nanowires. *Angew. Chem.*, *Int. Ed.* **2019**, *58* (45), 16077-16081. DOI: 10.1002/anie.201909109.
- (83) Chouhan, L.; Ito, S.; Thomas, E. M.; Takano, Y.; Ghimire, S.; Miyasaka, H.; Biju, V. Real-Time Blinking Suppression of Perovskite Quantum Dots by Halide Vacancy Filling. *ACS Nano* **2021**, *15* (2), 2831-2838. DOI: 10.1021/acsnano.0c08802.
- (84) Yuan, J.; Ling, X.; Yang, D.; Li, F.; Zhou, S.; Shi, J.; Qian, Y.; Hu, J.; Sun, Y.; Yang, Y.; et al. Band-Aligned Polymeric Hole Transport Materials for Extremely Low Energy Loss α-CsPbI3 Perovskite Nanocrystal Solar Cells. *Joule* **2018**, *2* (11), 2450-2463. DOI: 10.1016/j.joule.2018.08.011.
- (85) Zhang, X.; Huang, H.; Jin, L.; Wen, C.; Zhao, Q.; Zhao, C.; Guo, J.; Cheng, C.; Wang, H.; Zhang, L.; et al. Ligand-Assisted Coupling Manipulation for Efficient and Stable FAPbI(3) Colloidal Quantum Dot Solar Cells. *Angew. Chem., Int. Ed.* **2023**, *62* (5), e202214241. DOI: 10.1002/anie.202214241.
- (86) Xu, L.; Qiu, W.; Feng, M.; Liang, Z.; Qian, W.; Zhou, C.; Zhang, D.; Li, M.; Lv, W.; Tao, Y.; et al. Multifunctional Resonance Bridge-Mediated Dynamic Modulation of Perovskite Films For Enhanced Intrinsic Stability of Photovoltaics. *Small* **2023**, *19* (25), e2207226. DOI: 10.1002/smll.202207226.
- (87) Zhang, Y.; Xu, L.; Sun, J.; Wu, Y.; Kan, Z.; Zhang, H.; Yang, L.; Liu, B.; Dong, B.; Bai, X. 24.11% High Performance Perovskite Solar Cells by Dual Interfacial Carrier Mobility

Enhancement and Charge-Carrier Transport Balance. Adv. Energy Mater. 2022, 12 (37), 2201269.